JMEPEG (2022) 31:1–10
https://doi.org/10.1007/s11665-021-06142-z

1059-9495/$19.00

In Vitro Degradation Behavior of Ti-Microalloyed AZ31 Magnesium Alloy in Simulated Body Fluid

S. Candan, S. Emir, and E. Candan

Submitted: 11 December 2020 / Revised: 22 June 2021 / Accepted: 15 July 2021 / Published online: 26 August 2021

Corrosion and corrosion-related mechanical behaviors of Ti-microalloyed AZ31 Mg alloy (AZ31Ti) in simulated body fluid (SBF) under a dynamic environment were investigated. AZ31 Mg alloy was used as a control alloy. Microstructure analysis of the samples was performed by using a scanning electron microscope and an x-ray diffractometer. Mass loss measurements and corrosion-related tensile tests were carried out by immersing the samples in the SBF solution at 37.5 ± 0.5 °C for 24, 72, and 336 h under dynamic conditions. Potentiodynamic polarization and electrochemical impedance spectroscopy measurements were also employed in the SBF solution at 37.5 ± 0.5 °C. Microstructural studies showed that the β ($Mg_{17}Al_{12}$) intermetallic phases in the AZ31 alloy are dispersed in the microstructure and formed as relatively angular particles, and that the dimensions of the β phases transformed to a smaller size and globular form with Ti microalloying. While the tensile strength and hardness values of AZ31 and AZ31Ti alloys were similar to each other, Ti microalloying showed a considerable increase in the yield strength and elongation. This study suggests that microalloying of AZ31 alloy with Ti is beneficial in terms of their corrosion resistance and corrosion-related mechanical properties in an SBF environment under dynamic conditions.

Keywords AZ31 Mg alloys, biocorrosion, mechanical properties, simulated body fluid

1. Introduction

In recent years, Mg-based alloys have been a focus of degradable implant research due to their biodegradable, biocompatible, and better mechanical properties (Ref 1-3). Mg is harmless since the metallic ion (Mg^{2+}) released as a result of dissolution is the fourth most common cation in the human body, and its specific modulus is close to that of the human bone (Ref 4). Therefore, the potential for future use of these alloys as biodegradable metallic implant materials for plate and screw production in orthopedic implant applications is of interest (Ref 4-6). On the other hand, Mg corrodes very quickly in solutions containing chlorine (Cl^-), such as body fluid (Ref 5); therefore, the alloy loses its mechanical integrity with rapid hydrogen (H_2) gas accumulation before the tissue heals (Ref 7). Thus, it is crucial to improve the corrosion resistance of Mg alloys and to control their degradation for potential biomedical applications. In this respect, many investigations have been focused on the alloying design (Ref 8, 9) and post-treatment (Ref 10) of such alloys. Zhang et al. (Ref 9) stated that more attention should be paid to the corrosion mode and mechanical integrity rather than the corrosion rate for studying biodegradable Mg alloys. Particularly, the alloying design could be the most effective approach if the alloying elements are carefully selected and balanced in Mg alloys to enhance their corrosion resistance and mechanical integrity.

Commercially available Mg alloys need to be re-designed to be compositionally suitable for the human body since such alloys are currently designed for automotive and electronic industries. In this respect, various types of Mg-based alloying designs have been introduced for biomedical applications (Ref 5, 10-15). For example, the use of Ca and rare earth elements (Y, Ce, Pr, etc.) as an additional alloying element to AZ series Mg alloys (Mg-Al-Zn alloys) improve the biodegradability properties of these alloys (Ref 14, 16). It has been reported (Ref 16) that the addition of low Ca content (< 1 wt.%) improves the corrosion behavior of AZ91 alloy exposed to simulated body fluid (SBF), showing a plausible decrease in the ultimate tensile strength (UTS) and elongation (ε). On the other hand, a higher Ca content (> 1 wt.%) in Mg alloys can cause poor corrosion resistance (Ref 17). Li et al. (Ref 18) and Liu et al. (Ref 19) suggested that the increase in corrosion resistance of Ce added AZ91 alloy was attributed to suppressed microgalvanic corrosion in the alloys. Although Ce was reported to increase the corrosion resistance of AZ series alloys, it has been stated (Ref 20) that severe hepatotoxicity was observed in the body. Literature studies (Ref 8, 21, 22) show that, despite the beneficial effect of Al content in Mg alloys in terms of strength, it must be kept to a minimum level due to the risk of Alzheimer's disease. Therefore, studies (Ref 4, 5) on the development of Mg alloys with low amounts of Al have attracted much attention.

Biocorrosion-related degradation of Mg alloys for biomedical applications have mainly been investigated by exposing them in a static environment (Ref 23). However, considering the physiological flow conditions in the human body, experiments in a static environment may not reveal plausible results (Ref 23). Due to different corrosion behaviors of Mg alloys under dynamic and static conditions, recent research studies have focused on the flow-induced biocorrosion behavior of Mg

S. Candan, Department of Biomedical Engineering, Engineering Faculty, Necmettin Erbakan University, 42090 Meram, Konya, Turkey; **S. Emir**, Department of Mechanical Engineering, Bilecik Seyh Edebali University, Bilecik, Turkey; and **E. Candan**, Department of Metallurgy and Materials Engineering, Engineering Faculty, Necmettin Erbakan University, Konya, Turkey. Contact e-mail: sennur.candan@erbakan.edu.tr.

alloys (Ref 24, 25). Wang et al. (Ref 24, 26) investigated the corrosion behaviors of AZ31 stents and MgZnCa plates and reported that the flow rate significantly alters the corrosion behaviors of the alloys. Recent studies (Ref 25, 27) reported that the flow-induced biocorrosion behaviors of pure Mg porous orthopedic implants (in SBF) and AZ31 alloy coronary stents (in DMEM) under dynamic conditions was much higher than those in static conditions. Han et al. (Ref 28) investigated the influence of flow rate on biocorrosion of AZ31B alloy and reported that the corrosion rate of AZ31B alloy increased with increasing flow rate of both SBF and phosphate-buffered solution (PBS) under dynamic conditions.

Our previous studies (Ref 29, 30) and patent (Ref 31) have shown that the corrosion resistance and mechanical properties of Ti-microalloyed AZ series alloys improve significantly in a NaCl environment. Later, Choi and Kim (Ref 32, 33) reported similar results that microalloying of AZ series Mg alloys with Ti effectively improves their corrosion resistance in a NaCl environment. However, to the best of our knowledge, studies on the biodegradability properties of Ti-microalloyed AZ31 Mg alloy (AZ31Ti) in an in vitro environment have not been reported. Ti is also considered to be the most biocompatible metal in body environment. Therefore, the aim of this work is to investigate the corrosion and corrosion-induced mechanical behaviors of Ti-microalloyed AZ31 alloy in SBF solution under dynamic conditions.

2. Materials and Methods

Preparation of the alloy specimens were carried out by a casting process. For the casting process, Mg, Al, and Zn ingots (min. 99.90% purity) were used. Commercial grade Al-10Ti in stick form was used for Ti microalloying. The master alloying procedure was carried out by placing Mg and Al ingots together with the Al-10Ti alloy stick in a crucible (graphite) followed by melting under an Ar gas atmosphere at 750 °C, then pouring the molten alloy into a permanent mold. The addition of Zn was performed 1 min prior to the casting process in order to prevent Zn evaporation. The prepared master alloys were remelted, then cast into a preheated (~ 250 °C) cast iron permanent mold having a 22 mm diameter and a 220 mm length under a protective gas (SF_6) atmosphere. Table 1 illustrates the chemical compositions of the alloys obtained by using optical emission spectrometry (OES). All the specimens used in this work were in as-cast form.

For microstructural evaluation, samples having an approximately 18 mm diameter and 10 mm thickness were machined from the cast alloys. 220, 400, 600, 800, 1200, 2000, and 2500 sand emery papers were used for the grinding stage. Samples were then polished down to 1 µm with diamond-based paste.

Optical microscopy (OM) (Olympus/GX4) and scanning electron microscopy (SEM) (Zeiss Supra 40 VP) equipped with energy dispersive x-ray spectroscopy (EDS) were used for microstructural evaluation. The samples were etched in 5 g picric acid, 5 ml acetic acid, 10 ml distilled water, and 100 ml ethanol solution. The linear intercept method was used to determine the grain size of the alloys. X-ray diffraction (XRD) analysis (PAN analytical/ Empyrean diffractometer) was carried out under CuK_α radiation with the incidence beam angle of 2°. The diffraction angle range was between 20° and 80° with a step increment of 0.02° and a count time of 1 s.

Determination of micro hardness values were carried out by the Vickers (Shimadzu HMV-2) hardness test at 5 N load. Hardness values were recorded as an average of at least ten hardness measurements on each sample.

Tensile test samples were machined according to ASTM E 8M-99. For corrosion-related tensile tests, the samples were isolated thoroughly except for the gauge area to be exposed to the corrosion media. Photographs of the tensile samples for control and immersion tests are shown in Fig. 1. The isolation was performed by painting followed by tight covering with Teflon stripe thoroughly. Tensile tests were performed on the previously immersed tensile samples at a crosshead displacement rate of 0.25 mm/min at room temperature by using a Shimadzu AG-IS model testing machine. Each data represents an average of at least three samples in the tensile tests. The 0.002 strain offset method was used to calculate yield strength (YS).

The chemical composition of the corrosion media (i.e., SBF) with a volume of 1 L is composed of 8.035 g NaCl, 0.225 g KCl, 0.355 g $NaHCO_3$, 0.311 g $MgCl_2{\cdot}6H_2O$, 0.231 g $K_2HPO_4{\cdot}3H_2O$, 0.292 g $CaCl_2$, 39 mL 1.0M-HCl, 0.072 g Na_2SO_4, 6.118 g Tris, and 0-5 mL 1.0M-HCl, as proposed in Ref 34. Before the corrosion experiments, the pH of the solutions was adjusted to 7.4 ± 0.5.

For the immersion experiments, a dynamic test apparatus was designed and manufactured. The dynamic test apparatus consisted mainly of a corrosion medium reservoir, peristaltic pump, thermocouple, pH meter, heat bed, and real-time controlling unit, as shown schematically in Fig. 2. The corrosion medium volume in the reservoir was 1.5 L, corresponding to ~ 40 mL cm^{-2} sample surface area, and the solution temperature was adjusted to 37.0 ± 0.5 °C by an electronic controlling unit. The samples were placed in the center of the apparatus. The velocity of the solution flow was maintained by the peristaltic pump at approximately 0.336 cm s^{-1}, similar to the flow velocity reported in (Ref 28).

The mass loss measurement samples were machined and prepared with the similar sizes used for the microstructural examinations. Both the mass loss and corrosion-related tensile test samples were immersed together in the apparatus and exposed for 24, 72, and 336 h in SBF under the dynamic fluid condition. For the mass loss experiments, the sample surfaces were cleaned with deionized water followed by alcohol and their weight recorded prior to immersion.

The dynamic test apparatus was sealed with a tight lid to avoid evaporation of the fluid during the exposure period. The pH value was checked at 1 h intervals by the real-time

Table 1 Chemical compositions of AZ31 and AZ31Ti Mg alloys (wt.%)

Alloys	Al	Zn	Mn	Fe	Ni	Cu	Ti	Mg
AZ31	2.7	1.02	0.20	< 0.018	< 0.002	< 0.004	…	Rest
AZ31Ti	2.9	0.90	0.18	< 0.018	< 0.002	< 0.004	0.05	Rest

controller and maintained at around 7.4 ± 0.5 during the immersion period. When the pH value increased to ~ 8, 1.0 M HCl was added to the solution to maintain the pH at 7.4.

After the immersion tests, the mass loss samples were cleaned with 200 g L^{-1} CrO_3 solution for 15 min to remove the corrosion residuals followed by cleaning with deionized water, drying, and weighing. Sample weight loss was calculated in mg cm^{-2}, taking into account the total sample surface area. Hereinafter, this will be referred to as corrosion loss.

Potentiodynamic curves and electrochemical impedance spectroscopy (EIS) were performed by means of a Gamry model PC4/300mA potentiostat/galvanostat controlled by a computer with DC105 corrosion analysis software. A three-electrode cell configuration was used for the measurements, working electrodes (alloy samples), a platinum electrode as auxiliary, and a saturated Ag/AgCl/KCl reference electrode. In order to minimize the ohmic drop, a Luggin capillary was used. Electrochemical experiments were realized in a glass cell containing SBF solution at 37.0 ± 0.5 °C temperature under a static condition. The temperature of the glass cell containing the SBF solution was maintained by a heat bed controlled by an electronical unit. The impedance spectra were acquired by using a perturbation amplitude of ± 10 mV (vs. stabilized open circuit potential (OCP) after 1 h), and a frequency interval from 100 kHz to 50 mHz. Potentiodynamic scans were performed directly after the EIS tests, starting from − 0.5 to + 0.5 V versus OCP at a scan rate of 1 mV s^{-1}. Measurements were performed three times to ensure the reproducibility of the results.

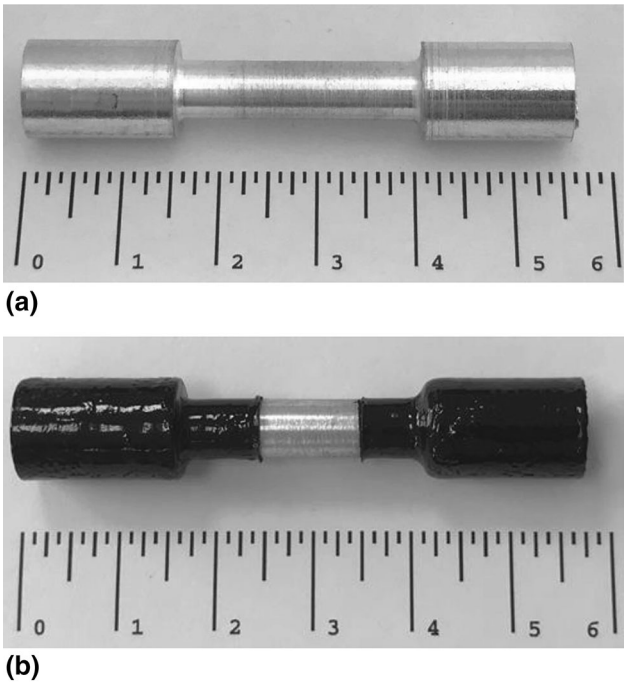

Fig. 1. Photographs of the tensile samples for (a) control and (b) immersion tests

3. Results and Discussion

3.1 Microstructure

Figure 3 presents OM micrographs of as-cast AZ31 and AZ31Ti alloys. It is evident that the Ti microalloying refined the microstructure of the AZ31 alloy. The mean grain size of the AZ31 alloy was ~ 110 µm, whereas it was reduced to ~ 68 µm with Ti microalloying of the AZ31 alloy.

SEM microstructures of AZ31 and AZ31Ti Mg alloys, together with their EDS analysis at selected areas, are illustrated in Fig. 4. Mainly, two different phases were distinguished alongside with α-matrix; eutectic morphology and nodular-like bright phase. According to the EDS results, the intermetallic phases with eutectic morphologies (#9-14 in Fig. 4a and #11-15 in Fig. 4b) have the compositions equivalent to the β ($Mg_{17}Al_{12}$) phase in accord with literature (Ref 35, 36) on as-cast AZ31 alloys. When the Mg-Al phase diagram is examined (Ref 37), the eutectic β phase occurs as the Al rate in the Mg matrix rises above 13 wt.% under equilibrium cooling conditions. However, in the non-equilibrium cooling conditions, i.e., during casting, the eutectic structure of Al can occur even at around 2 wt.%. (Ref 38). As reported previously (Ref 29, 30, 39), fully, partially, and/or lamellar eutectic β phases

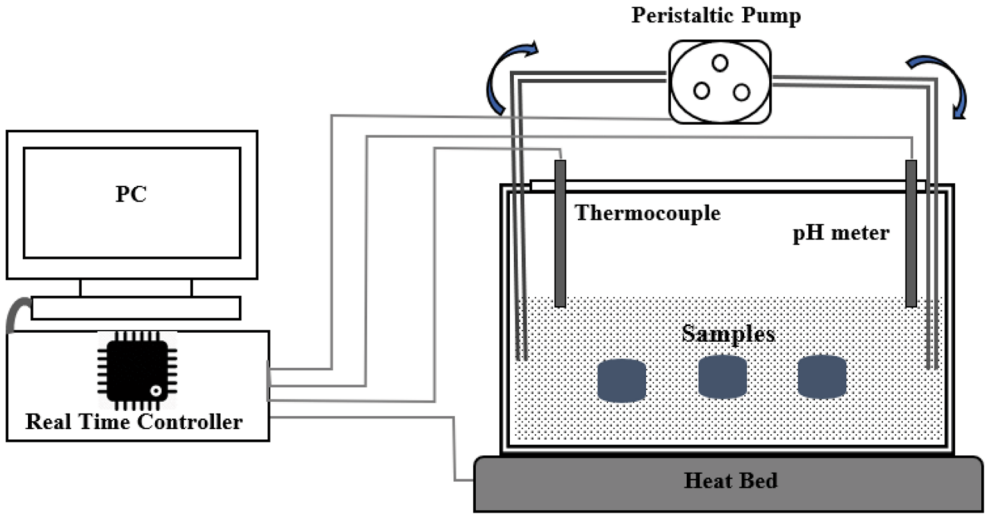

Fig. 2. Schematic of the dynamic test apparatus in vitro

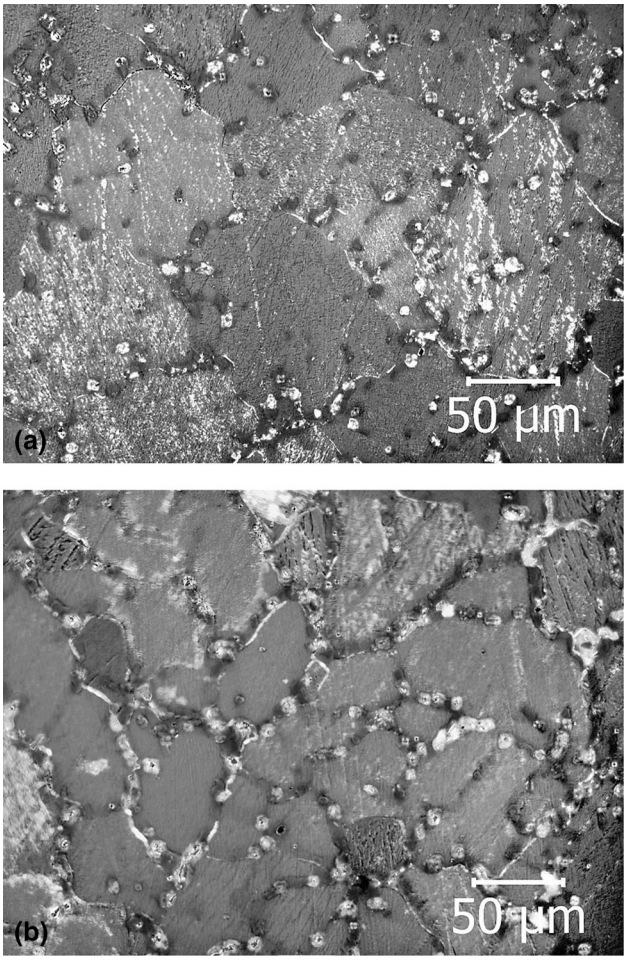

Fig. 3. Optical microstructures of as cast (a) AZ31 and (b) AZ31Ti alloys

occur in AZ series Mg alloys depending on their Al ratios and solidification conditions. The β phase has formed, along the grain boundaries and in the α-Mg matrix, as an $Mg_{17}Al_{12}$ intermetallic compound. In the initial stages of solidification, the enrichment of Al in front of the dendrite arms occurs due to the constitutional undercooling and the segregation tendency of Zn. Formation of the eutectic β phase within α-Mg could occur owing to the enriched Al in front of the dendrites. XRD diffractograms of both alloys shown in Fig. 5 indicate that α-Mg could be clearly detected; however, the β phase could not be identified due to the low ratio of Al in the alloy. Similar results have also been reported in the work of Wang et.al. (Ref 11), which showed that identifying the β phase was difficult in AZ31 alloys by XRD analysis owing to the low amount of β phase in the microstructure. When high magnification SEM microstructures of AZ31 and AZ31Ti alloys are compared, β phases in the Ti-containing alloy show finer, smaller grain size and relatively spherical forms in the microstructure (Fig. 6). This was attributed to the grain refining effect of Ti on the α-grain structure. Choi and Kim (Ref 32) also reported similar results that the addition of Ti (0.007%) to AZ31 alloy refined the grain structure, in agreement with the present study. At the same time, the EDS results for the nodular-like bright phases (#5-8 in Fig. 4a and #6-10 in Fig. 3b) show that they are composed of Al and Mn, which was thought to be Al_8Mn_5 phase (Ref 36). Furthermore, it has been reported (Ref 36) that

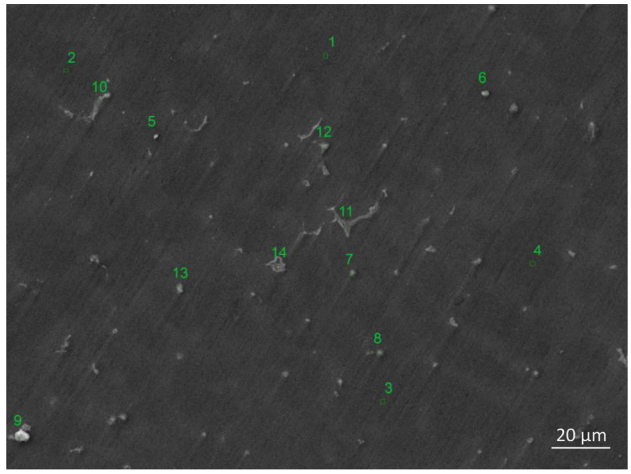

Area/Element (Mean, wt.%)	Al	Zn	Mn	Mg
#1-4 (α-Matrix))	1.18	0.31	0.23	Rest
#5-8 (Bright, Nodular)	39.22	2.08	44.44	Rest
#9-14 (Eutectic-like)	22.13	20.21	-	Rest

(a)

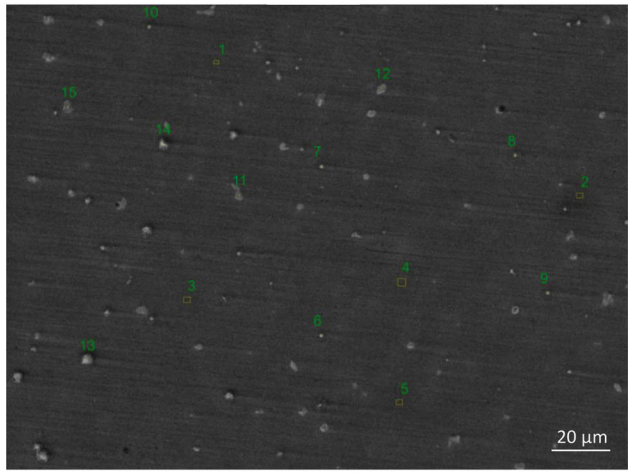

Area/Element (Mean, wt.%)	Al	Zn	Mn	Ti	Mg
#1-5 (α-Matrix)	1.70	0.34	0.12	0.04	Rest
#6-10 (Bright, Nodular)	45.4	1.11	53.5	-	Rest
#11-15 (Eutectic-like)	22.70	24.02		-	Rest

(b)

Fig. 4. Microstructures and EDS analysis of (a) AZ31 and (b) AZ31Ti alloys (Magnification: 500 X)

the $Mg_{21}(Zn, Al)_{17}$ phase in the AZ31 as-cast Mg alloys could exist alongside with the β phase.

From our previous works (Ref 29, 30), adding a small amount of Ti ($< 0.5\%$) to AZ91 alloy plays three roles. Firstly, the addition of Ti refines the dendritic structure and grain size. Ti in the Mg matrix limits the rate of dendritic growth during solidification (Ref 40). During solidification, Ti probably increases the constitutional undercooling at the solid/liquid interface, thus ensuring that the dendrites are finer and the formation of smaller grains accordingly. Zhao et al. (Ref 40) and Choi and Kim (Ref 32, 33) showed that adding even a trace amount of Ti (0.0013-0.0037%) caused refinement of the grain

size and a secondary phase in the Mg alloy. Secondly, the addition of Ti promotes the formation of the fully divorced β phase while suppressing the formation of the lamella eutectic β phase. There are similar results that the addition of a small amount of Ti to AZ61 and AZ91 alloys reduce the content of partially divorced and lamella eutectic β phases (Ref 33, 41, 42). Thirdly, the addition of Ti increases the Al solubility in the

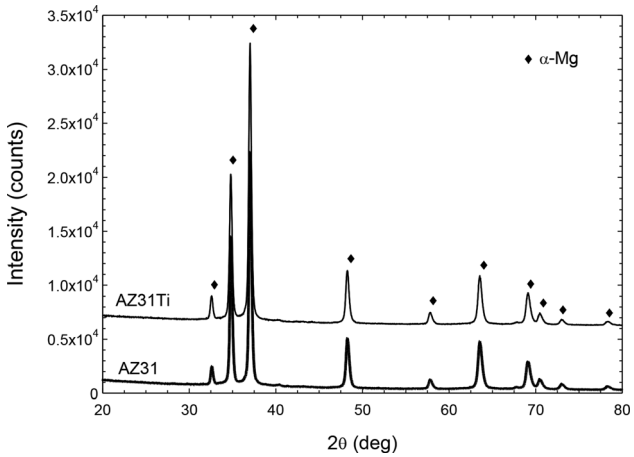

Fig. 5. XRD patterns of AZ31 and AZ31Ti alloys

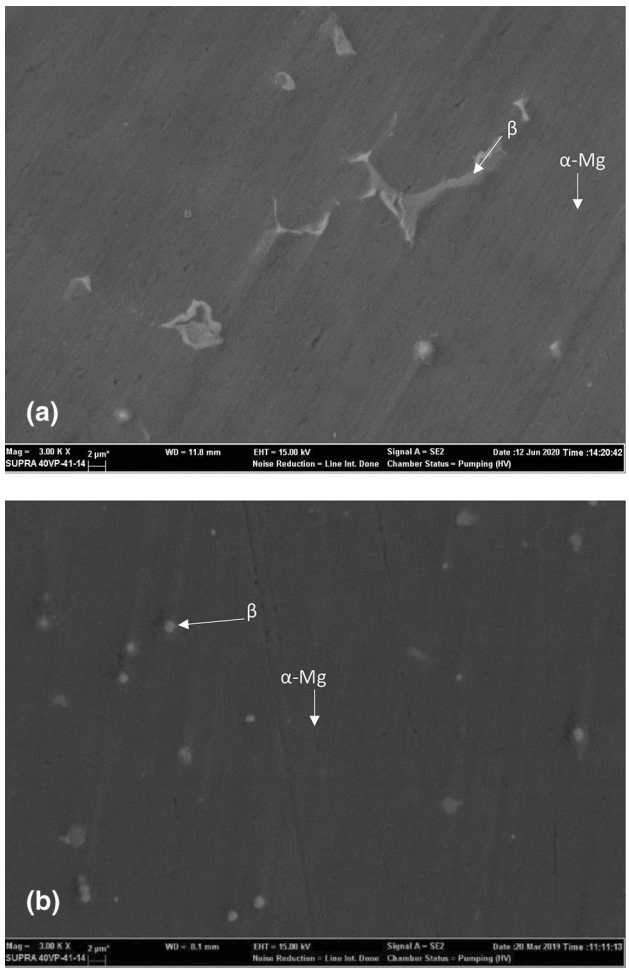

Fig. 6. SEM morphology of secondary phases in (a) AZ31 and (b) AZ31Ti alloys

α-Mg matrix phase (Ref 29, 30, 32, 33). It is evident from EDS analysis that the average Al amount in α-Mg within the AZ31 alloy is 1.18 wt.%, whereas it is 1.70 wt.% in the AZ31Ti alloy (see Fig. 4a, b). These results are entirely consistent with our previous study (Ref 29) and the works of Choi and Kim (Ref 32, 33).

3.2 Mechanical Tests

The tensile stress–strain curves for both AZ31 and AZ31Ti alloys are shown in Fig. 7. Ti microalloying improved the yield strength (YS), ultimate tensile strength (UTS), and elongation (ε) of the AZ31 alloy (Fig. 7). The hardness (HV), UTS, YS, and ε values of both alloys are also given in Table 2. Microalloying of the AZ31 alloy with Ti did not result in any significant change in HV and UTS values, whereas an improvement of 18% in YS and 23% in ε has been achieved. The increase in YS and ε of the AZ31Ti alloy was attributed to the finer grain size and relatively spherical forms of β phase in the microstructure, as explained earlier. It is believed that the lower YS and ε in the AZ31 alloy are mainly caused by the coarse grains and casting defects. The similar HV values between the AZ31 and AZ31Ti alloys may also be due to the casting defects (i.e., porosity, microshrinkage, etc.).

3.3 Corrosion Behavior

Corrosion loss results of the AZ31 and AZ31Ti alloys are given in Fig. 8. In the short exposure time (i.e., up to 24 h), both control and AZ31Ti alloys showed similar corrosion losses, whereas in the long-term immersion test (i.e., 336 h), a considerable improvement was observed in the corrosion resistance by Ti microalloying of the AZ31 alloy. Corrosion loss of the AZ31 alloy for 336 h was 74 mg cm^{-2}, while it was 54 mg cm^{-2} for the AZ31Ti alloy, leading to an improvement in the corrosion loss of up to $\sim$ 27%. Mena-Morcillo (Ref 43) studied corrosion loss of AZ31 alloy in SBF for 168 h and reported the corrosion loss of AZ31 alloy as 3.53 mg cm^{-2}. Discrepancies between the present work and the work of Mena-Morcillo (Ref 43) was attributed to manufacturing and experimental conditions. They (Ref 43) used rolled AZ31 alloy sheet samples in their work, whereas in the present work, the samples were in as-cast condition. In addition, corrosion loss measurements in the present work were under a dynamic condition, which may lead to an increased corrosion loss as compared to a static environment (Ref 43). In Fig. 9, cross-

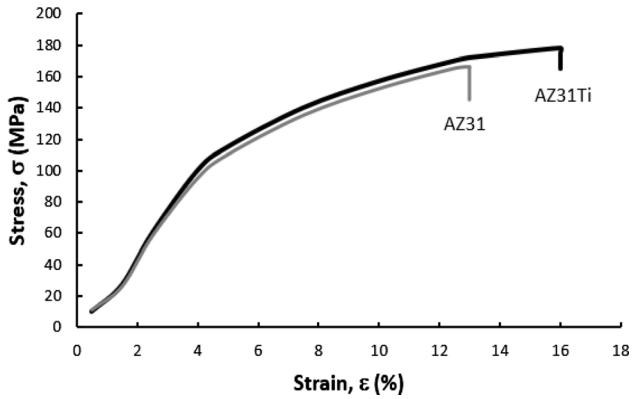

Fig. 7. The tensile stress–strain curves for AZ31 and AZ31Ti alloys

Table 2 Results of microhardness and tensile properties of cast AZ31 and AZ31Ti alloys

Alloys	$HV_{0.5}$	YS, MPa	UTS, MPa	ε, %
AZ31	50 ± 7	98 ± 14	173 ± 16	13 ± 5
AZ31Ti	51 ± 4	116 ± 9	178 ± 12	16 ± 4

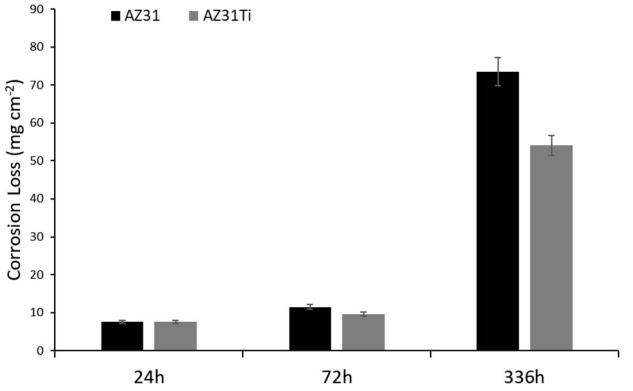

Fig. 8. Corrosion losses of AZ31 and AZ31Ti alloys exposed to SBF solution for 24, 72, and 336 h

sectional SEM microstructures of AZ31 and AZ31Ti alloys exposed to an SBF environment for 72 and 336 h are shown. It is clear that the AZ31 alloy is subjected to more severe corrosion compared to the AZ31Ti alloy at a prolonged exposure time, as shown in Fig. 9(c)-(d).

Since the strength is equal to the force divided by the area, as the corrosion proceeds, the cross-sectional area of the sample also decreases, which leads to obtain the real cross-sectional area of the degraded sample extremely difficult. Therefore, the strengths of the alloys given here should be considered as the forces it can bear. Force at rupture (strength) of AZ31 and AZ31Ti alloys obtained after immersion in SBF medium for 72 and 336 h is given in Fig. 10. Photographs of the tensile samples for AZ31 and AZ31Ti alloys after the immersion (72 and 336 h) tests are shown in Fig. 11. Before the immersion tests, the forces at rupture of the AZ31 and AZ31Ti alloys were 4889 N and 5030 N, respectively. Their rupture forces are reduced to 2487 N and 2543 N, respectively, after immersion for 72 h. With further increasing immersion time (i.e., 336 h), a dramatic reduction in their forces (1215 and 1978 N) were observed. These results show that both alloys lose their mechanical strength in the immersion experiments. However, in the prolonged immersion tests (i.e., 336 h), the Ti-microalloyed AZ31 alloy showed much better mechanical properties (i.e., ∼ 60%) compared to that of the AZ31 control alloy. It is thought that the reason for the better mechanical properties for the AZ31Ti alloy in the long-term immersion tests may be due to corrosion progress on the surface of the alloy. In the prolonged immersion time, corrosion has progressed deeper toward the inner part of the AZ31 control sample, whereas the progression was much less pronounced in the AZ31Ti sample (Fig. 9). As corrosion advances deeper toward the inner section of the sample, it decreases the unit surface area leading to a decreased force. In addition, the larger size of the notches formed due to prolonged corrosion could be another factor in creating crack sites. Zhang et al. (Ref 9) reported that the

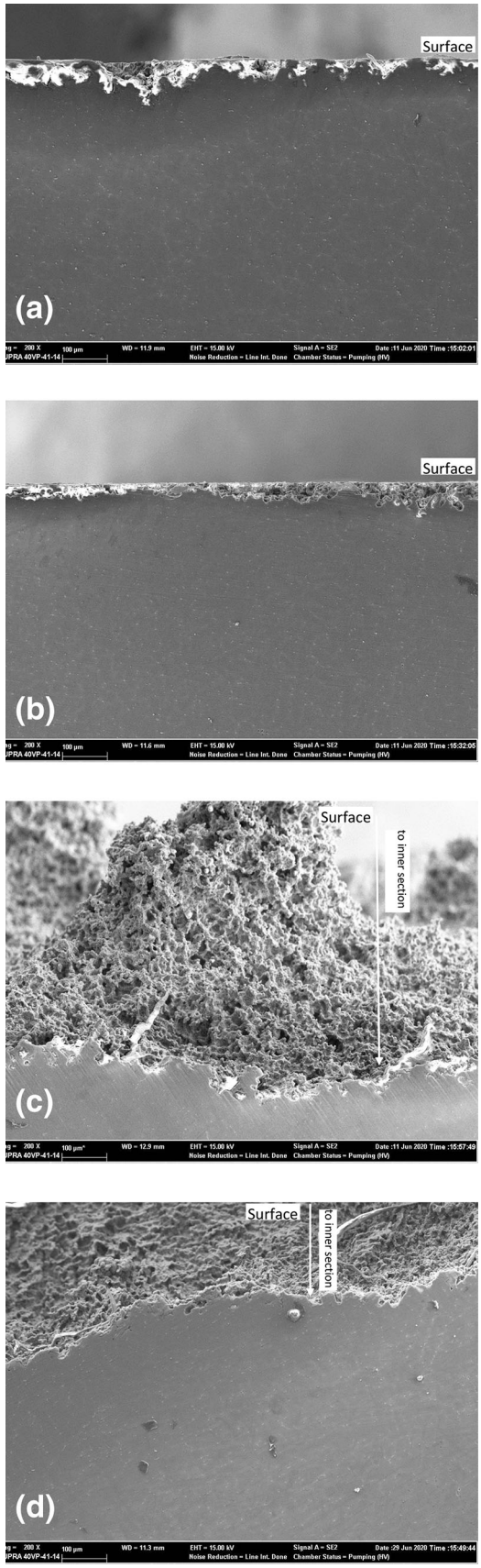

Fig. 9. Cross-sectional SEM images of the samples immersed in SBF for 72 h ((a) AZ31, (b) AZ31Ti) and for 336 h ((c) AZ31, (d) AZ31Ti)

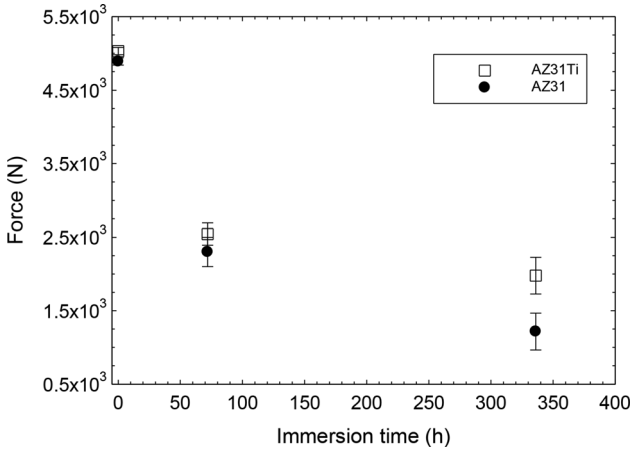

Fig. 10. Rupture force of AZ31 and AZ31Ti alloys after 72 and 336 h immersion in SBF solution

mechanical degradation of the GZ60K and GZ61K alloys showed a decrease as the duration of immersion increased in SBF, which is in agreement with the present work. However, compared to the present work, a slight decrease was observed in their work. This may be due to the composition, microstructure, and manufacturing processes.

Potentiodynamic polarization curves for AZ31 and AZ31Ti Mg alloys in SBF medium are shown in Fig. 12, and their I_{corr} and E_{corr} values obtained from the polarization curves are given in Table 3. The I_{corr} values of AZ31 and AZ31Ti alloys are 126 and 97 μA cm^{-2}, respectively. Compared to the AZ31 alloy, the Ti microalloying resulted in a slight negative shift of the E_{corr} value, whereas its I_{corr} values decreased. This indicates that AZ31 is more prone to being thermodynamically stable against corrosion, but in terms of kinetics, AZ31 corrodes faster. A promising alloying addition does not necessarily raise the E_{corr} of the alloy to a more noble potential but rather shows a lower corrosion rate (Ref 44). In this study, Ti addition, which improves the overall corrosion resistance, does, in fact, lower E_{corr} (more active) while decreasing the corrosion rate, in accordance with the works of Sudholz et al. (Ref 44) and Choi and Kim (Ref 32). I_{corr} values of the present work do not agree with the works of Bertolini et al. (Ref 45) and Mena-Morcillo (Ref 43), who investigated the corrosion of AZ31B alloy in SBF. Bertolini et al. (Ref 45) reported the I_{corr} value of AZ31B alloy as 10 μA cm^{-2}, while Mena-Morcillo (Ref 43) reported the I_{corr} value of AZ31B alloy as 52 μA cm^{-2}. This may be due to the impurities (i.e., Fe, Cu, Ni, etc.) in the alloy (Ref 46) as well as manufacturing variables of the AZ31 alloys that were used. Manufacturing variables, such as solidification conditions of the melt (Ref 30), machining parameters (Ref 45), etc., significantly affect the corrosion behavior of AZ series alloys. Fig. 13 shows the Nyquist plots of both AZ31 and AZ31Ti alloys. The larger the radius of the loop, the better is the corrosion resistance. The AZ31Ti alloy has larger capacitive loops than the AZ31 alloy, indicating that Ti microalloying increases the corrosion resistance of the AZ31 alloy.

Compared to the AZ31 control alloy, the higher corrosion resistance of the AZ31Ti alloy could be based on three interrelated reasons. The first reason is grain refinement and the β phase in the microstructure; corrosion generally occurs at the vicinities of both grain boundaries and secondary particles (i.e., β phase). The mean grain size of the AZ31 alloy decreased from ~ 110 to ~ 68 μm with the Ti microalloying (Fig. 3). The amorphous region at the grain boundaries causes a potential difference, which leads to an increased corrosion rate. It is expected that the potential difference in the amorphous area around fine grains should be less compared to coarse grains. In our previous study (Ref 30), it was reported that the corrosion resistance of AZ91 alloy increased with increasing melt cooling rate attributed to the refinement of grain size. On the other hand, the volume fraction and morphology of the β phase could be another influence. As discussed in the microstructure section, the Ti microalloying increases the Al

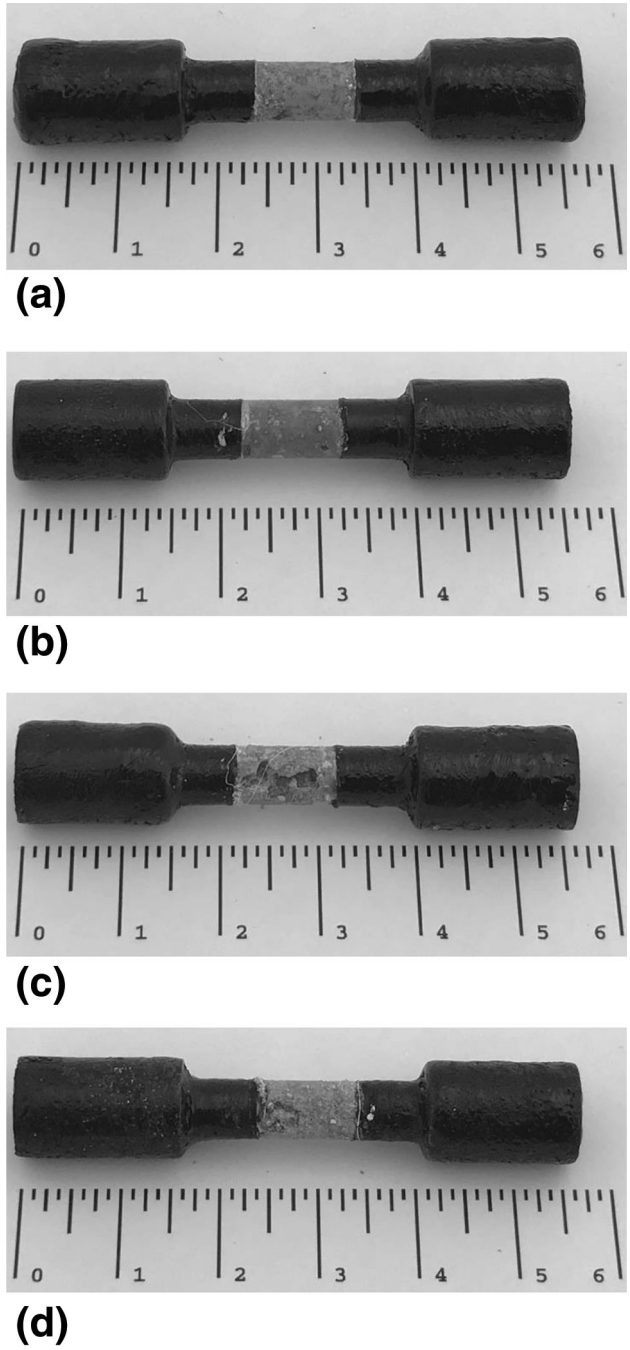

Fig. 11. Photographs of the tensile samples immersed in SBF for 72 h ((a) AZ31, (b) AZ31Ti) and for 336 h ((c) AZ31, (d) AZ31Ti)

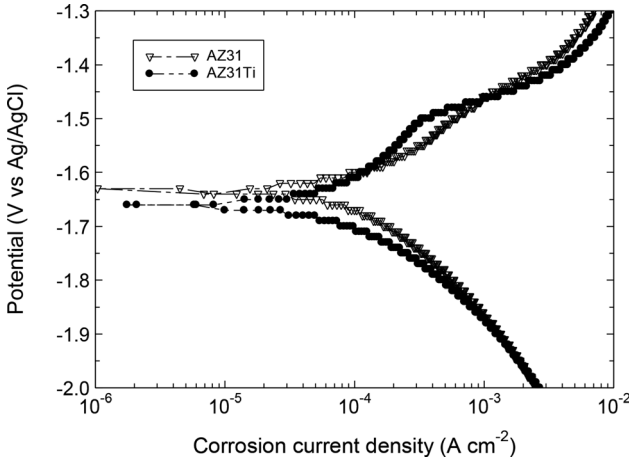

Fig. 12. Potentiodynamic polarization curves for AZ31 and AZ31Ti alloys in SBF solution

Table 3 E_{corr}, I_{corr}, and CR values of AZ31 and AZ31Ti alloys derived from the polarization curves

Alloys	E_{corr}, mV	I_{corr}, $\mu A/cm^2$	CR, mm/y
AZ31	− 1632 ± 20	126 ± 22	2.9
AZ31Ti	− 1660 ± 25	97 ± 15	2.2

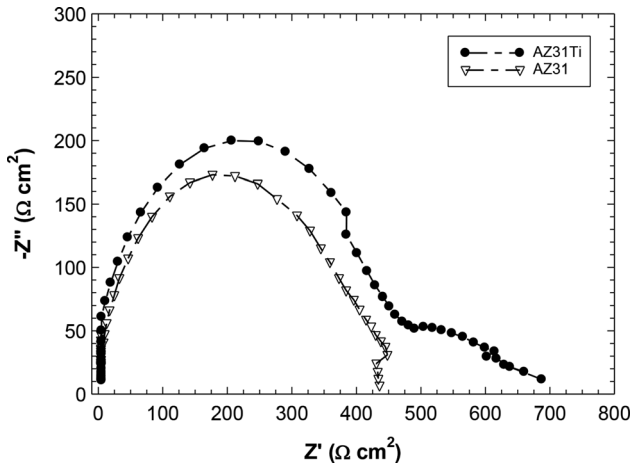

Fig. 13. Nyquist plots of AZ31 and AZ31Ti in the SBF solution

solubility in the α-Mg matrix phase. This should reduce the volume fraction of the β phase to be formed during solidification in the AZ31Ti alloy. A decrease in the volume fraction of the β phase by Ti addition to AZ series Mg alloys has been reported in our previous works (Ref 29, 30) and the works of Choi and Kim (Ref 32, 33). Choi and Kim (Ref 41) reported that AZ61 alloys containing 0.02 wt.% Ti exhibited better corrosion resistance than the 0.01 wt.% Ti-added alloy, attributed to a decreased volume fraction and size of the β phase, which reduced the galvanic corrosion effect. This is in accord with the present work. Additionally, compared to the AZ31 alloy, the β phase in the Ti-containing alloy formed as finer and relatively spherical forms in the microstructure, as shown in Fig. 6. Initially, corrosion takes place in the α-matrix at the vicinity of the β phase, then the β phase falls off, resulting in large corrosion losses at a prolonged immersion time. In the AZ31 alloy, the bigger grain size and the coarser β phase with higher volume fraction are involved and thus, the non-uniform corrosion occurs, leading to a higher corrosion current density. As for the AZ3Ti alloy, the β phase is finer and globular in the α-matrix, and more uniform corrosion is involved. In agreement with the present work, Gong et al. (Ref 13) reported that the smaller size and more dispersed β along the grain boundaries resulted in more uniform corrosion in the Mg-4Zn alloy containing up to 0.2% Sr. When the Sr content was above 0.2%, secondary phase particles were coarsened, which deteriorated the corrosion.

The second reason is possibly due to the morphology and continuity of the oxide film formed on the alloy surfaces. In our previous study (Ref 39) on the corrosion behavior of AZ series alloys, it was reported that the morphology of the β phase and the oxide film formed on the surface caused different effects between the initial stages of corrosion and the prolonged exposure stages. Semi-passive $Mg(OH)_2$ oxide film is formed on the surface of Mg and its alloys in aqueous environments, and the hydration of the MgO converts the cubic MgO to hexagonal $Mg(OH)_2$ having a volume twice that of the oxide (Ref 47). On the other hand, a quantitative XPS study (Ref 47) on the surface films formed on Mg and Mg-Al intermetallics revealed that the oxide film on β intermetallics forms as $AlMgx(OH)y$, and the film growth rates on the β intermetallics were much faster than those on α-Mg. Disruption of the semi-protective layer may take place more easily on the coarsened β phase owing to differences in volume changes between the different oxides on the α-Mg matrix and the β intermetallics, as explained in Ref (Ref 39). Taking into account the dynamic conditions in the present work, disruption of the oxide film may be more severe.

The third reason could be the formation of an Al_2O_3 layer between the quasi-passive film and the surface of the alloy. As reported by Song et al. (Ref 48) and Esmaily et al. (Ref 49), the oxide film on the AZ series Mg alloy consists of three layers: an inner layer (rich in Al_2O_3), a middle layer (mainly MgO), and an outer layer ($Mg(OH)_2$). They suggested that the positive effect of Al in the Mg alloy on improved corrosion properties was due to the formation of an Al_2O_3 layer at the inner part acting as a passive film between the quasi-passive film and the surface of the alloy. In our previous work (Ref 29, 30) and the works of Choi and Kim (Ref 32, 33), as well as in the present work, the increase in Al content in the α-phase by Ti addition is evident. The presence of increased Al content in α-Mg, promoted by Ti microalloying, probably augments the formation of the Al_2O_3 oxide film on the surface of the alloy, improving its resistance to the aggressive attack of Cl^- ions. It can be suggested that better in vitro corrosion resistance of the AZ31 alloy could be achieved with Ti microalloying owing to a less interrupted oxide film due to the formation of a finer grain size and β phase as well as increased Al content in α-Mg.

4. Conclusion

Corrosion and corrosion-related mechanical behaviors of Ti-microalloyed AZ31 Mg alloy exposed to 24, 72, and 336 h in SBF solution under a dynamic condition were investigated. The

main conclusions from the experimental analysis that can be drawn are as follows:

- Microstructural studies demonstrated that coarser β phases in the AZ31 alloy transformed to a smaller size and globular form with Ti microalloying.
- While the UTS and HV values of AZ31 and AZ31Ti alloys were close to each other, Ti microalloying showed a considerable increase in the YS and ε. The improved ductility and yield strength of the AZ31Ti alloy were attributed to the combination effect of grain refinement and modification of the β phase.
- Corrosion loss experiments showed that the AZ31 alloy has less corrosion resistance than that of its microalloyed version, which is consistent with the trend of the potentiodynamic polarization results.
- Increased corrosion resistance of the AZ31 alloy by Ti addition is attributed to the increased Al content in the α-phase, which augments the formation of the Al_2O_3 oxide film on the surface of the alloy as well as modifies the beta phase in the microstructure.
- The Ti-microalloyed AZ31 alloy showed improved corrosion-induced strength loss in the prolonged immersion tests, which was attributed to a relatively interrupted corrosion progress toward the inner part of the alloy.
- The study suggests that microalloying of AZ31 alloy with Ti is beneficial in terms of their corrosion-related mechanical properties and degradation resistance in an SBF environment under dynamic conditions.

Acknowledgments

This work has been funded by Bilecik Seyh Edebali University, Grant No: 2018-01.BŞEU.03-02. The authors would like to thank Fethi Candan for construction of the real-time dynamic corrosion test apparatus.

References

1. J. Chen, L. Tan, X. Yu, I.P. Etim, M. Ibrahim and K. Yang, Mechanical Properties of Magnesium Alloys for Medical Application: A review, *J Mech Behav Biomed.*, 2018, **87**, p 68–79
2. S. Amani and G. Faraji, Processing and Properties of Biodegradable Magnesium Microtubes for Using as Vascular Stents: A Brief Review, *Met Mater Int.*, 2019, **25**, p 1341–1359
3. N. Sezer, Z. Evis, S.M. Kayhan, A. Tahmasebifar and M. Koç, Review of Magnesium-Based Biomaterials and Their Applications, *J. Magnes. Alloys*, 2018, **6**, p 23–43
4. S. Agarwal, J. Curtin, B. Duffy and S. Jaiswal, Biodegradable Magnesium Alloys for Orthopaedic Applications: A review on Corrosion Biocompatibility and Surface Modifications, *Mater. Sci. Eng. C*, 2016, **68**, p 948–963
5. F. Witte, V. Kaese, H. Haferkamp, E. Switzer, A. Meyer-Lindenberg, C.J. Wirth and H. Windhagen, In vivo Corrosion of Four Magnesium Alloys and the Associated Bone Response, *Biomaterials*, 2005, **26**, p 3557–3565
6. G. Yuan and J. Niu, Research Progress of Biodegradable Magnesium Alloys for Orthopedic Applications, *Acta Metall. Sin.*, 2017, **53**, p 1168–1180
7. K. Pichler, S. Fischerauer, P. Ferlic, E. Martinelli, H.P. Brezinsek, P.J. Uggowitzer, J.F. Loffler and A.M. Weinberg, Immunological Response to Biodegradable Magnesium Implants, *JOM*, 2014, **66**, p 573–579
8. Y. Chen, J. Dou, H. Yu and C. Chen, Degradable Magnesium-Based Alloys for Biomedical Applications: The Role of Critical Alloying Elements, *J. Biomater. Appl.*, 2019, **33**, p 1348–1372
9. X. Zhang, J. Dai, Q. Dong, Z. Ba and Y. Wu, Corrosion behavior and Mechanical Degradation of as-Extruded Mg-Gd-Zn-Zr Alloys for Orthopedic Application, *J. Biomed. Mater. Res. B*, 2020, **1088**, p 698–708
10. Y. Sasikumar, A.M. Kumar, R. Suresh-Babu, P. Dhaiveegan, N. Al-Aqeeli and A.L.F. de Barros, Fabrication of Brushite Coating on AZ91D and AZ31 Alloys by Two-Step Chemical Treatment and Its Surface Protection in Simulated Body Fluid, *J. Mater. Eng. Perform.*, 2019, **28**, p 3803–3815
11. X.J. Wang, D.K. Xu, R.Z. Wu, X.B. Chen, Q.M. Peng, L. Jin, Y.C. Xin, Z.Q. Zhang, Y. Liu, X.H. Chen, G. Chen, K.K. Deng and H.Y. Wang, What is Going on in Magnesium Alloys?, *J. Mater. Sci. Technol.*, 2018, **34**, p 245–247
12. M.B. Kannan, Influence of Microstructure on the in-vitro Degradation Behaviour of Magnesium Alloy, *Mater. Lett.*, 2010, **64**, p 739–742
13. X. Gong, J. Chen, H. Yan, W. Xia, B. Su, Z. Yu and H. Yin, Effects of Minor Sr Addition on Biocorrosion and Stress Corrosion Cracking of As-Cast Mg-4Zn Alloys, *Corrosion*, 2020, **76**, p 71–81
14. K. Gusieva, C.H.J. Davies, J.R. Scully and N. Birbilis, Corrosion of Magnesium Alloys: The Role of Alloying, *Int. Mater. Rev.*, 2015, **60**, p 169–194
15. Y. Ding, C. Wen, P. Hodgson and Y. Li, Effects of Alloying Elements on the Corrosion Behavior and Biocompatibility of Biodegradable Magnesium Alloys: A Review, *J. Mater. Chem. B*, 2014, **2**, p 1912–1933
16. M.B. Kannan and R.K.S. Raman, In Vitro Degradation and Mechanical Integrity of Calcium-Containing Magnesium Alloys in Modified-Simulated Body Fluid, *Biomaterials*, 2008, **29**, p 2306–2314
17. G. Wu, Y. Fan, H. Gao, C. Zhai and Y.P. Zhu, The Effect of Ca and Rare Earth Elements on the Microstructure, Mechanical Properties and Corrosion Behaviour of AZ91D, *Mater. Sci. Eng. A*, 2005, **408**, p 255–263
18. Z. Li, X. Gu, S. Lou and Y. Zheng, The Development of Binary Mg-Ca Alloys for use as Biodegradable Materials Within Bone, *Biomaterials*, 2008, **29**, p 1329–1344
19. Y. Liu, Q. Wang, Y. Song, D. Zhang, S. Yu and X. Zhu, A study on the Corrosion Behavior of Ce-Modified Cast AZ91 Magnesium Alloy in the Presence of Sulfate-Reducing Bacteria, *J. Alloys Compd.*, 2009, **473**, p 550–556
20. N. Hort, Y. Huang, D. Fechner, M. Stormer, C. Blawert, F. Witte, C. Vogt, H. Drucker, R. Willumeit, K.U. Kainer and F. Feyerabend, Magnesium Alloys as Implant Materials-Principles of Property Design for Mg–RE Alloys, *Acta Biomater.*, 2010, **6**, p 1714–1725
21. P.C. Ferreira, K.A. de Piai, A.M. Takayanagui and S.I. Segura-Muñoz, Aluminum as a Risk Factor for Alzheimer's Disease, *Lat. Am. Enfermagem*, 2008, **16**, p 151–157
22. H.R. Bakhsheshi-Rad, M.H. Idris, M.R. Abdul-Kadir, A. Ourdjini, M. Medraj, M. Daroonparvar and E. Hamzah, Mechanical and Bio-Corrosion Properties of Quaternary Mg-Ca-Mn-Zn Alloys Compared with Binary Mg-Ca Alloys, *Mater. Des.*, 2014, **53**, p 283–292
23. J. Gonzalez, R.Q. Hou, E.P.S. Nidadavolu, R. Willumeit-Römer and F. Feyerabend, Magnesium Degradation under Physiological Conditions-Best Practice, *Bioact, Mater.*, 2018, **3**, p 174–185
24. J. Wang, Y. Jang, G. Wan, V. Giridharan, G.L. Song, Z. Xu, Y. Koo, P. Qi, J. Sankar, N. Huang and Y. Yun, Flow-Induced Corrosion of Absorbable Magnesium Alloy: In-situ and Real-Time Electrochemical Study, *Corros. Sci.*, 2016, **104**, p 277–289
25. A.P. Md Saad, R.A. Abdul Rahim, M.N. Harun, H. Basri, J. Abdullah, M.R. Abdul Kadir and A. Syahrom, The influence of Flow Rates on the Dynamic Degradation Behaviour of Porous Magnesium Under a Simulated Environment of Human Cancellous Bone, *Mater. Des.*, 2017, **122**, p 268–279
26. T. Wang, D. Kevorkov, A. Mostafa and M. Medraj, Experimental Investigation of the Phase Equilibria in the Al-Mn-Zn System at 400 °C, *J. Mater.*, 2014, **2014**, p 1–13
27. Y. Koo, T. Tiasha, V.N. Shavov and Y. Yun, Expandable Mg-based Helical Stent Assessment using Static, Dynamic, and Porcine Ex Vivo Models, *Sci. Rep.*, 2017, **7–1173**, p 1–10
28. L. Han, X. Lib, J. Baia, F. Xuea, Y. Zhengc and C. Chu, Effects of Flow Velocity and Different Corrosion Media on the in Vitro

Biocorrosion Behaviors of AZ31 Magnesium Alloy, *Mater Chem Phys.*, 2018, **217**, p 300–307
29. S. Candan, M. Unal, E. Koc, Y. Turen and E. Candan, Effects of Titanium Addition on Mechanical and Corrosion Behaviours of AZ91 Magnesium Alloy, *J. Alloys Compd.*, 2011, **509**, p 1958–1963
30. S. Candan, M. Celik and E. Candan, Effectiveness of Ti-Micro Alloying in Relation to Cooling Rate on Corrosion of AZ91 Mg Alloy, *J. Alloys Compd.*, 2016, **672**, p 197–203
31. E. Candan, S. Candan, M. Unal, Y. Turen and E. Koc, High Strength and Corrosion Resistant Mg alloys Microalloyed with Ti or/and Pb, Turkish Patent Office, Patent No TR 2008 09986 B, 2008
32. H.Y. Choi and W.J. Kim, Development of the Highly Corrosion Resistant AZ31 Magnesium Alloy by the Addition of a Trace Amount of Ti, *J. Alloys Compd.*, 2016, **664**, p 25–37
33. H.Y. Choi and W.J. Kim, The Improvement of Corrosion Resistance of AZ91 Magnesium Alloy Through Development of Dense and Tight Network Structure of Al-Rich a Phase by Addition of a Trace Amount of Ti, *J. Alloys Compd.*, 2017, **696**, p 736–745
34. T. Kokubo and H. Takadama, How Useful is SBF in Predicting in Vivo Bone Bioactivity?, *Biomaterials*, 2006, **27**, p 2907–2915
35. H. Zhao, P. Li and L. He, Microstructure and Mechanical Properties of an Asymmetric Twin-Roll Cast AZ31 Magnesium Alloy Strip, *J. Mater. Process Technol.*, 2012, **212**, p 1670–1675
36. L. Wu, F. Pan, M. Yang and R. Cheng, An Investigation of Second Phases in as-Cast AZ31 Magnesium Alloys with Different Sr Contents, *J. Mater. Sci.*, 2013, **48**, p 5456–5469
37. H. Baker, Alloy Phase Diagrams, *ASM Handbook*, 1998, **3**, p 280
38. I. Polmear, D.S. John, J.F. Nie, M. Qian, Light Alloys, 5th Edn., Butterworth-Heinemann, Oxford, 2017
39. S. Candan and E. Candan, Comparative Study on Corrosion Behaviors of Mg-Al-Zn Alloys, *Trans. Nonferrous Met. Soc. China*, 2018, **28**, p 642–650
40. P. Zhao, Q. Wang, C. Zhai and Y. Zhu, Effects of Strontium and Titanium on the Microstructure, Tensile Properties and Creep Behavior of AM50 Alloys, *Mater. Sci. Eng. A*, 2007, **444**, p 318–326
41. J.Y. Choi and W.J. Kim, Significant Effects of Adding Trace Amounts of Ti on the Microstructure and Corrosion Properties of Mg-6A-1Zn Magnesium Alloy, *J. Alloys Compd.*, 2014, **614**, p 49–55
42. X. Ai and G. Quan, Effect of Ti on the Mechanical Properties and Corrosion of Cast AZ91 Magnesium Alloy, *Open Mater. Sci. J.*, 2012, **6**, p 6–13
43. E. Mena-Morcillo and L. Veleva, Degradation of AZ31 and AZ91 Magnesium Alloys in different Physiological Media: Effect of Surface Layer Stability on Electrochemical Behaviour, *J. Magnes. Alloys*, 2020, **8**, p 667–675
44. A.D. Sudholz, N. Birbilis, C.J. Bettles and M.A. Gibson, Corrosion Behaviour of Mg-alloy AZ91E with Atypical Alloying Additions, *J. Alloys Compd.*, 2009, **471**, p 109–115
45. R. Bertolini, S. Bruschia, A. Ghiottia, L. Pezzatoa and M. Dabalàa, The Effect of Cooling Strategies and Machining Feed Rate on the Corrosion Behavior and Wettability of AZ31 Alloy for Biomedical Applications, *Procedia CIRP*, 2017, **65**, p 7–12
46. S. Candan, S. Cim and E. Candan, Effectiveness of Ti Micro-Alloying for the Suppression of Fe Impurities in AZ91 Mg Alloys and Associated Corrosion Properties, *Mater. Test.*, 2019, **61**, p 1165–1170
47. M. Liu, S. Zanna, H. Ardelean, I. Frateur, P. Schmutz, G. Song, A. Atrens and P. Marcus, A first Quantitative XPS Study of the Surface Films Formed, by Exposure to Water, on Mg and on the Mg–Al Intermetallics: Al_3Mg_2 and $Mg_{17}Al_{12}$, *Mater. Sci. Eng. C*, 2016, **68**, p 948–963
48. G.L. Song and A. Atrens, Corrosion Mechanisms of Magnesium Alloys, *Adv. Eng. Mater.*, 1999, **1**, p 11–33
49. M. Esmaily, D.B. Blücher, J.E. Svensson, M. Halvarsson and L.G. Johansson, New Insights into the Corrosion of Magnesium Alloys-The Role of Aluminum, *Scr. Mater.*, 2016, **115**, p 91–95